Mechanical and molecular activation lead to structurally analogous MscL states

Bolin Wang[1,2,3], Benjamin J. Lane[1,2,3], Charalampos Kapsalis[4], James R. Ault[2,5], Frank Sobott[2,5], Hassane El Mkami[6], Antonio N. Calabrese[2,5], Antreas C. Kalli[2,7], Christos Pliotas*[,2,3,4]

[1]Equal first author contribution

[2]Astbury Centre for Structural Molecular Biology, University of Leeds, UK

[3]School of Biomedical Sciences, Faculty of Biological Sciences, University of Leeds, UK

[4]Biomedical Sciences Research Complex, School of Biology, University of St Andrews, UK

[5]School of Molecular and Cellular Biology, Faculty of Biological Sciences, University of Leeds, UK

[6]School of Physics and Astronomy, University of St Andrews, UK

[7]Leeds Institute of Cardiovascular and Metabolic Medicine, School of Medicine, University of Leeds, UK

* Corresponding author: Christos Pliotas, c.pliotas@leeds.ac.uk

Author Contributions: C.P. conceived and designed the project. B.W., B.J.L, C.K., J.A., H.E.M., A.C.K. and C.P. performed research. B.W., B.J.L, C.K., J.A., F.S., H.E.M., A.N.C., A.C.K. and C.P. processed and analysed data. C.P. wrote the manuscript assisted by B.W., B.J.L. with contributions from H.E.M, A.N.C. and A.C.K.

Competing Interest Statement: The authors declare no conflicts of interest

Classification: Biological Sciences/Biophysics and Computational Biology

Keywords: MscL, mechanosensitive channels, EPR, HDX, ESEEM

This PDF file includes:

Main Text

Figures 1 to 7

Tables 1 to 1

Abstract

The mechanosensitive channel of large conductance MscL gates in response to tension changes in the membrane to allow the exchange of molecules through its pore. Native ligands that bind and modulate MscL are unknown and trapping an activated state has been challenging. Disruption of lipid access to tension-sensitive transmembrane pockets by modification leads to a concerted structural and functional MscL response. However, it is unknown whether there is structural correlation between tension mediated and molecular activation in mechanosensitive channels. Here, we combine HDX mass spectrometry and ESEEM solvent accessibility measurements on MscL, coupled with molecular dynamics under bilayer tension, to investigate the structural changes associated with the two distinctively derived states. Membrane thinning is not sufficient to hydrate

the MscL pore, when lipids are trapped in the pockets, under tensions capable to gate the native channel. Tension and molecule stabilised states present analogous MscL structures, suggesting a link between these two distinct activation mechanisms. These findings could hint at synergistic modes of regulation in mechanosensitive ion channels with implications for their multimodality.

Significance Statement

Bacterial mechanosensitive channels are gated by membrane tension and their function is modulated by lipids or molecules binding to tension sensitive domains. Eukaryotic mechanosensitive channels are multimodal and regulated both by tension and molecular triggers. However, whether molecular and tension activation present mechanistic similarities and whether such mechanisms have evolved through converged structural plasticity of a common origin is largely unclear. Here we use the mechanosensitive channel of large conductance MscL and compare its two distinctive gating dynamics by experimental (EPR and HDX-MS) and computational means (MD). We find that these two differently derived states are structurally analogous suggesting links between mechanosensitivity and ligand-gating in the regulation of mechanosensitive channels and with implications for their multimodality.

Main Text

Introduction

Mechanosensitive (MS) ion channels can sense and respond to tension changes in the cell membrane. Lipids are important for the folding, stability and structural integrity of membrane proteins (1), while structural responses mediated through lipid binding to exposed protein domains are allosterically linked to their regulation (2-4). Several models place the lipids as central to the allosteric regulation of membrane proteins (3, 5-10). Previously, hydrophobic pockets formed within transmembrane (TM) domains of bacterial MS channels have been proposed to play a role in the transduction of bilayer forces to the channel, directly forming pressure-sensitive domains, or pockets (2, 3, 5). These were first identified on the MS channel of small conductance MscS, leading to the lipid moves first hypothesis, which predicts that lipids access these pockets and apply pressure to the channel gate to keep it closed (5). When a modification (L89W) was introduced at the entrance of these pockets in MscL, lipid contacts with the backside of the pore-lining helices were reduced, generating a structural response in the absence of applied tension (2). Such a model suggests that molecular triggers could act as negative allosteric modulators and that tension could be mimicked by molecules in order to activate MS channels (2, 3).
Indeed, the function of MscL (11-13) and MscS (5, 14) can be modulated by molecule occupancy changes within these pockets. Subtle structural differences within the same regions lead to substantial functional differences in orthologous MscL proteins (15). This suggests a common regulatory mechanism, tailored to the unique structural landscape of MS channels, which may guide ligand specificity (2, 3).
In mammals, the MS channel Piezo1 is activated by Yoda1, opening up the possibility of endogenous agonists (16, 17), while TRAAK and TREK-1 are responsive to natural chemical ligands including arachidonic acid, polyunsaturated fatty acids, and lysophosphatidic acid (18-21). Lipids residing within similar inner-leaflet pockets have also been linked with mechanosensitivity in x-ray and cryo-EM structures of TRPV3 (22), TRAAK (23), TREK-2 (24) and MscS (25), while their unique parallel to membrane plane orientation may be guided by an amphipathic helix that is important for mechanosensitivity in MscL (26) and GPCRs (27). Pulsed electron-electron double resonance (PELDOR, also known as DEER) and x-ray studies on the LmrP multidrug transporter

showed that lipids could provide a hydrophobic counterpart to partially fill binding pockets and participate in the coordination of ligand binding(28).
Attempts to model MscL opening have been previously implemented via steered MD simulations, with pulling tensions (29-33) an order of magnitude higher than the ones required to open MscL in giant unilamellar vesicles (GUVs) and spheroplasts (2, 34, 35). In other cases MscL was subjected to substantial modifications or forces were applied for short periods of time (29, 36-38). MD simulations on TREK-2 have shown that under increase bilayer tension the channel moves from a "down" to an "up" configuration accompanied by cross sectional area changes, while its pockets are occupied by lipids only in the absence of membrane stretch (39). Therefore, it seems that the channel kind of "snaps open", unless it is pushed shut via lipids.
Hydrogen Deuterium eXchange Mass Spectrometry (HDX-MS) and 3 pulse Electron Spin Envelope Echo Modulation (3pESEEM) spectroscopy are powerful tools in the investigation of membrane protein structural dynamics. The former involves the exchange of protons on a protein with deuterium generates accessibility information and has been used to provide key insights into the role of lipids in determining the conformational state, but also secondary structure changes in membrane transporters (40-44). The latter measures weak hyperfine coupling between unpaired electrons and nuclear spins to probe accessibility to solvent (D_2O) and protons (residues, ions and lipids) and has been used to investigate the dynamics of membrane proteins (2, 15, 45-51).
We hypothesized that there is a link between the physiologically relevant tension-activated state, and the one stabilized by molecular triggers, and investigated whether there is structural analogy between these two states. Here, we combine untargeted (HDX-MS) and single-residue (3pESEEM) with molecular trigger activation (by modifying the pocket entrance with a bulky amino acid substitution, L89W) on MscL and independently generate a tension-activated state by MD simulations to interrogate whether there is a link between the two differently derived states. We find these states are structurally analogous, suggesting an intimate relationship between tension- and ligand- activation in MS channels, potentially linked to their functional multimodality.

Results

Channel gating by molecular activation monitored by HDX-MS

The substitution of a bulky tryptophan residue at position L89 in the Mycobacterium tuberculosis MscL (TbMscL) has been shown to restrict lipid access to channel pockets and destabilised the closed state, leading to an expanded (sub-conducting) MscL state(2). In order to give a mechanistic insight into the transitions occurring between the two states, we used HDX-MS to measure relative differences in deuterium uptake between the WT (closed) and L89W (expanded by molecular activation) channels in DDM. We succeeded in obtaining 95% peptide coverage of the entire resolved MscL structure where the gating occurs, i.e. residues 1-125, including the entire TM domain and the largest part of the cytoplasmic helical bundle (83% overall coverage for the entire construct including the C-terminal 6xHis-tag). Differences in uptake, detected at the peptide level, between the two states allowed us to identify protein regions that became deprotected from exchange in the sub-conducting L89W state (Fig 1). Three regions of MscL were identified and showed significant changes between the two states. Peptides in the regions containing residues 37-53 (periplasmic loop) and, 58-69 (top of TM2), and 97-111 (bottom of TM2, cytoplasmic loop and top of the cytoplasmic helical bundle) had a significantly higher uptake of deuterium in L89W in comparison to WT TbMscL (Fig 1, S1 and Table S1). Residues 37-53 run from the top of TM1 and end after the first β-sheet in the loop connecting TM1 to TM2. Residues 58-69 correspond to the middle of the periplasmic loop up until TM2, and residues 97-111 cover the bottom of TM2 to the top of the C-terminal helical bundle (Fig 1 and S1). This gave us the first glimpses into which MscL domains are mostly impacted by the L89W (pocket entrance) modification across MscL's length.

Solvent accessibility mapping at single residue resolution by 3pESEEM

We first aimed to investigate the feasibility of 3pESEEM on MscL and identify potential dynamic sites. To this end, we generated twenty-six single cysteine mutants, accounting for over 20% of the

total TbMscL resolved length, spanning all protein domains. In particular, L2 and F5 on the S1 helix, N13, L17, V21, I23, V31 and F34 on TM1, L42, and F48 on the periplasmic loop, residues N70, V71, L72, L73, A74, F79, F84, A85, Y87, F88, L89, R98, K99, and K100 on TM2, and E102 and V112 on the cytoplasmic loop and helical bundle (CHB) respectively, were mutated in the Cys-free WT TbMscL as the background (Fig 2). We subsequently expressed, purified and spin labelled each one of these twenty-six mutants (MTSSL modification is denoted as R1 thereafter) and performed 3pESEEM solvent accessibility measurements, based on the modulation depth of deuterium in the time domain signal, which is proportional to its associated signal intensity in the frequency domain. Unlike PELDOR which requires high spin labelling efficiency to obtain high sensitivity data acquisition (2), 3pESEEM can be performed with no major losses in sensitivity even if the samples of interest show lower spin labelling efficiencies for individual sites. This has allowed us to obtain good quality spectra and quantify the solvent (D_2O) accessibility for all twenty-six sites. Residues in the S1 helix showed low accessibility, which is consistent with previous reports suggesting that this helix is buried within the bilayer (53). TM1 pore-lining residues presented low to intermediate accessibility (Fig 2 and S2), as would be expected for a closed channel pore (2, 54, 55). I23, V31 and F34 on TM1 are intermediately solvent-exposed (or relatively buried) and positioned on the same side of TM1 (Fig 2 and S2). This could be due either to the presence of native lipids, DDM and/or hinderance by the presence of TM2 on the TM1 interface. L42 and V48 are intermediately to highly exposed, as they form part of the periplasmic loop connecting TM1 and TM2. N70, V71, L72, L73, and A74 present the largest disparity across our whole data set. L72 is the most buried residue we measured (~ 3% compared to the most solvent-exposed cytoplasmic-facing labelled residue K100R1) while N70 (~90%) and V71 (~80%) are two of the most exposed (~90%), comparable to D_2O (solvent) accessibilities measured for exposed cytoplasmic sites (Fig 2 and S2). The rest present intermediate accessibilities to these two extremes, as expected for subsequent residues, which form a helical turn with different space orientation. Residues N70 and V71 are solvent-exposed in the closed MscL state, while residues L72 and L73 are buried. The latter pair of residues is known to become exposed during opening, due to an anti-clockwise TM2 rotation (2, 56). F79, F84 and A85 are relatively buried and lie at the interface of TM helices between different MscL subunits. Y87 has been identified as a lipid binding site (57) and along with F88 and L89 presented low to intermediate accessibilities and forms part of the pocket region (2, 15). Except for R98, which showed intermediate accessibility, K99 and K100, presented high accessibilities, indicating these residues are solvent-exposed in the closed state. These three residues form a positively charged cluster for attracting negatively charged lipids (57) and our data suggest that the non-ionic DDM binds either differently or at a different site. Substitution of these residues with the neutral Gln had no effect on MscL's conformation, suggesting that specific lipid headgroup binding on this particular site does not influence MscL gating (2). E102 (cytoplasmic loop) and V112 (cytoplasmic helical bundle) presented high solvent accessibility as it would be expected for cytoplasmic sites.

Identification of channel gating regions with single residue resolution

HDX-MS resolution is usually limited to the peptide level and, therefore, is unable to resolve changes that occur at different residues within the same peptide. Solvent accessibility can be probed at the single residue level using 3pESEEM allowing us to examine the relative solvent accessibility of individual residues. This generates higher resolution information pertaining to the regions of structural change identified by HDX-MS, as well as to the channel pore vapour lock. In each of these regions, we introduced eight distinct single cysteine substitutions in an L89W MscL background. Specifically, N13 and V21 (pore), L42 in the periplasmic loop, N70, V71, L72, L73 (top of TM2) and K100 (bottom of TM2 and cytoplasmic loop) (Fig 3). V21 forms the vapour lock (along with L17) that controls the channel gate and N13 sits one turn of a helix below. No significant change in this region was highlighted via HDX-MS, while due to the close proximity of spin labels pointing towards the pore (Fig S3), distances are out of PELDOR's distance measurement range (>20 A). However, 3pESEEM is highly sensitive to the local spin label environment of specific sites, does not need a reference channel state as it is the case for HDX-MS, and is not subjected to distance restrictions as PELDOR. Differences in the vapour-lock region may not have been

192 detected by HDX-MS as structural changes may have resulted in complex changes to hydrogen
193 bonding networks, whereby some residues were deprotected from exchange and others became
194 protected, resulting in only minor/no changes in deuterium uptake at the peptide level (Fig 1). To
195 resolve this, we labelled the crucial V21 site and N13, and six other sites within the regions identified
196 by HDX-MS, which undergo conformational changes when the L89W modification is present (Fig
197 3). N13R1's side chain points towards the cytoplasm and is expected to be solvent-exposed in the
198 closed state (Fig S2 and S3). Overall, the motivation behind this was to confirm the peptide-level
199 HDX-MS data and complement this with single residue resolution data for cases where crucial sites
200 have been undetected potentially due to limitations imposed by peptide-level HDX-MS analysis.
201 3pESEEM measurements at positions N13 and L42 showed no significant difference in solvent
202 accessibility between the WT and the L89W background. In L89W, the accessibility increased for
203 V21, which is consistent with a pore hydration, and an over ten-fold increase observed for L72. A
204 significant decrease was observed for K100 though, which sits at the C-terminal end of TM2 (Fig
205 3). A decrease in solvent accessibility was observed for N70 and V71 in presence of the
206 modification (molecular activation) with 2.4% and ~19% reduction, respectively. Despite being
207 consecutive residues, 70-73 show distinct changes in solvent accessibility in 3pESEEM, unlike
208 HDX-MS, which averages across the top of TM2 region and relies on single peptide coverage of
209 these residues. A significant and smaller increase in accessibility is seen for L72 and L73, and
210 opposite to the effect observed for N70 and V71, while the bottom of TM2 (K100) becomes less
211 accessible to solvent in the L89W background (Fig 3). This result is consistent with a rotation of the
212 top of TM2 which occurs during mechanical activation and agrees with PELDOR distance
213 measurements and x-ray structures (2, 15, 56). HDX-MS experiments showed deprotection on
214 peptides inclusive of these residues and is consistent with a dramatic increase in accessibility of
215 residue L72 for L89W in 3pESEEM measurements (Fig 3). V21R1 forms the vapour-lock for
216 TbMscL and shows an increase in solvent accessibility in an L89W background, consistent with
217 the pore gate hydration and the channel entering a sub-conducting state. HDX-MS measurements
218 show a deprotection of the TM2 bottom for L89W versus WT suggesting an overall solvent
219 exposure of this region (Fig 1 and 3). The MscL cytoplasmic loop has been shown to participate
220 in gating and provide access to streptomycin for entering the cell, while shortening of the loop
221 influences MscL's function by irreversibly decreasing its conductance (13, 58).
222
223 **Membrane tension stretching promotes pore hydration in the WT channel**
224 In order to mimic the naturally occurring activation of MscL and estimate how far the proposed
225 transitions determined in DDM micelles are comparable to simulated transitions in a lipid
226 membrane, we implemented MD simulations on the WT TbMscL, with tension and no tension
227 applied to the lipid bilayer. We performed the no tension simulations within the same lipid
228 composition in order to compare the pore properties and overall channel architecture between
229 these states. Our simulations were initiated from the TbMscL X-ray structure (PDB 2OAR)(55)
230 carrying no modifications. Previously, significantly higher bilayer tension was required to open MscL
231 in MD simulations over short periods of simulation time(29-31), in comparison to the lower tension
232 (~67.5 mN/m) and longer simulation times (300 ns) used in this study, allowing us to capture
233 intermediate states.
234 WT TbMscL was inserted in a POPC bilayer and simulations for 300 ns were performed in which
235 the x- and y- pressure of the box was set at -50 bars constant bilayer tension. During the
236 simulations, the bilayer could expand in order to adopt the membrane expansion occurring in the
237 xy plane. As a result the bilayer thickness decreased approximately 1.2 nm compared to the POPC
238 bilayer without tension (Fig 4). The channel underwent large conformational changes reaching an
239 overall RMSD of ~14 Å compared to the initial closed structure (Fig S4A) to adapt to the changes
240 in the bilayer by tilting its TM helices towards the xy plane (Fig 4A and Video S1). In particular, TM1
241 and TM2 gradually tilted by 30 and 15 degrees respectively towards the end of the simulations,
242 while the pressure-sensitive pocket surface and the area exposed to the bilayer decreased
243 dramatically (Fig 4, S4B and C).
244 Analysis of pore hydration profiles using CHAP (59) showed opening and hydration of the WT
245 channel pore under tension in all of our simulations (Fig 5A). Whilst the higher (compared to

biologically relevant) membrane tension does not allow us to provide information about the timescales of the channel transition from the closed to the hydrated state, it enables us to obtain structural data for an important intermediate state, which has a hydrated open pore, essential in MscL's gating process. For these pore hydration events we monitored the annular lipids, which make direct contact or reside in close proximity to the channel and simultaneously interrogated the pore radius profile using HOLE(60) (Fig 5B,C and 6C). We first observed that following constant tension application for ~200 ns, the pore becomes hydrated and the channel undergoes major structural rearrangements (Fig 5A). Although a significant membrane thinning (~1.2 nm) occurs during tension application, L89W's pore cannot open to allow water molecules to flow through and the pore radius is still restricted to ~1 Å, even though the changes in global secondary structure are similar to WT channel under tension (Fig 5 B,C,S4 and Table S2). Following bilayer stretching the total pocket surface area decreases and limits access and availability to bilayer lipids throughout our simulations (Fig 5B). Overall, the under tension MD data agree well with the HDX-MS and 3pESEEM accessibility data obtained for L89W (molecular activation). In both cases, similar channel regions become accessible to solvent suggesting a similar opening mechanism for the obtained expanded and sub-conducting state.

Safety-pin acting trapped lipids in the pockets do to allow for pore hydration

A direct consequence of the lipid moves first model would be that if lipids are trapped within and cannot become loosely associated with the pockets, under bilayer tension, the channel will not be able to open. To test this hypothesis we performed MD simulations with L89W TbMscL under tension and identical to WT conditions (POPC lipid bilayer, tension value and simulation time). L89W under tension undergoes similar global structural changes to the WT. However, its pore does not become hydrated, even under the tension conditions which previously promoted WT pore hydration (Fig 5A, 7B, S4 and Table S2).

During the equilibration of our simulations lipids intercalated into the pockets and occupied them. Following tension application, lipids were pulled towards the membrane, but the bulky tryptophan modification at the entrance disrupted the lipid exit path, despite tension application sufficient to open the WT channel was applied (Fig 5).

Interestingly, in the tension activated state, F79 and L89 from adjacent subunits come very close to form two new smaller pockets in the inner- and outer- leaflets of the now substantially thinner membrane (Fig 5C and D). This spatial "refinement" may facilitate the next stage in MscL's activation, which follows this sub-conducting state, that requires highly localised pressure for full opening of 3 nS and ~30 Å (2, 34, 35). Asymmetry in bilayer tension sensitivity has been observed for other mammalian mechanosensitive channels (61). Further, we observed that inner-leaflet lipids which could previously occupy MscL's pockets and keep the channel closed, now could penetrate either of the two newly created sub-pockets (Fig 5B and 6 A,B).

This change restricts the access of new lipids from the bulk membrane to the pockets, and immobilizes trapped lipids within the pockets that entered initially during equilibration. In such a case these lipids should interact more strongly with residue 89 in the modified (W89) than the WT (L89) channel. To test this hypothesis we calculated the pairwise energy forces between all lipids and residue 89, L and W, for the WT and modified channels respectively (Table 1). We found that the lipid interaction (Lennard-Jones) with residue 89 are twice as strong in the modified compared to WT channel (Table 1). This finding suggests that lipids are "stuck" by the modification in the pockets, reducing their ability to exchange with the bulk bilayer during tension application (Fig 3C and D). Despite the substantial global channel rearrangements L89W undergoes, lipids remain tightly associated with the pockets and the pore cannot hydrate (Fig 5).

Lipid order and contact accessibility changes during tension application

To assess the lipid contact profile with the MscL TM domain we calculated the relative difference of lipid contacts between the under- and no tension TbMscL states (Fig 6 and S5). We found that the relative lipid contacts within bilayer facing residues on the TM domain were reduced over the course of the simulation. In contrast, the lipid contacts of hydrophobic residues that were not lipid exposed in the closed state increased substantially (Fig 6 and S5). This is consistent with TM2

rotation occurring during MscL opening (2) and with pockets decreasing their surface contact area and becoming less accessible to lipids during opening (Fig 4B). To understand lipid rearrangement occurring upon tension application we calculated the lipid order before and after tension application. We found that all lipids (particularly the lipid chain ends) orient substantially more horizontally and that the pocket lipids specifically orient marginally more horizontal compared to the bulk bilayer lipids in the presence of tension (Fig S6).

Discussion

According to the lipid moves first model (5), MS channels open when lipids reduce contacts with the pockets. Equally, the model predicts that if lipids are trapped within the pockets, then the channel will not be able to open. Following application of bilayer tension to WT and L89W channels, we observe similar global structural rearrangements. Despite this, only the WT channel pore increased in diameter enough for pore hydration. The pore of the L89W channel was significantly smaller in volume and diameter. (Fig 2,3,5,6C and S4). Previously, when lipids were disrupted from entering the pockets, due to the L89W mutation located at the pocket entrance, the pore opening probability increased and the activation threshold significantly decreased (2). In the present set up, the L89W mutation locks the exit door and traps the lipids in the pockets by applying twice as strong steric forces which constrict the space for lipids to move out, compared to L89 in the WT channel (Fig 6A, B and Table 1). Lipids are also present in the pockets in the “hydrated” WT, following tension activation, but these are relatively loose and are not sufficient to close the channel (Fig 5B, 6B and Table 1). We find that the pockets become substantially smaller under tension and consequently less accessible to lipids (Fig 4B, 5B and 6). In the modified channel, F79 and W89 form a “molecular” bridge resulting in a two-compartment repartitioning of the smaller pockets (Fig 6A and B). The WT (under tension) expanded state is substantially different from the closed state x-ray structure used (PDB 2OAR) (Fig 4, S4 and Video S1). Importantly, TM2 movement (translation and expansion due to anticlockwise TM2 rotation) under tension is similar to that occurring upon molecular activation. When lipids are disrupted from entering the pockets, the state generated is similar to the archaeal x-ray expanded MscL model (56), which is also consistent with the expanded (and sub-conducting) L89W state, revealed by PELDOR (2) (Fig 7A). The L89W (molecular) and WT (tension) activated states are similar (Fig 7A), suggesting that MscL’s gating (from closed to expanded) is independent of the trigger used.

Previously, cross-sectional expansions, not associated to a conducting pore have been proposed for the initial stages of MscL activation (33, 62), suggesting MscL could act as a membrane tension dampener and undergo through closed-closed pore conformations (63). Our accumulative experimental (structural and biophysical) and computational data are in agreement with these models. Our data support the notion that there are structural transitions that occur prior to channel opening. Support is also provided for intimate lipid interactions with TM pockets that act as pressure safety pins to keep the channel closed until a certain tension threshold is reached (2). This was substantiated further when the channel was unable to gate after the lipids were trapped within these pockets via the L89W modification (Fig 5). Despite undergoing large conformational changes consistent with those seen for WT under tension, the trapped lipids prevent pore hydration and stabilize a closed (non-hydrated pore) but expanded state (Fig 3, 5, 7).

Our data suggest that for MscL to reach a hydrated state, promoted either by tension or molecular triggers, the lipids will have to loosen their contacts with the pockets (Fig 5 and Table 1). Lipids could move under tension and adopt a more horizontal orientation in respect to the membrane plane in the WT channel, in the absence of pocket modifications that disrupted lipid exchange with the bulk bilayer (Fig S6). The addition of molecules which could compete for the pockets may support or disrupt lipids acting as negative allosteric modulators within the pocket sites (Fig 7C). Following similar modifications at MscL’s pocket entrance, or when molecules that specifically bind these pockets were introduced, they caused a reduction in MscL’s activation threshold, prolonged openings and increased open channel probability (2, 12, 64).

Disruption of lipid access into the TbMscL’s pockets promoted a mechanical response in the absence of applied tension (2), while subtle structural differences between these pockets in MscL

354 orthologues dramatically altered their function (15). This pocket region in TbMscL, which is
355 important for lipid binding (2, 15), also binds, specific to EcMscL molecules, which could modulate
356 its activity (12, 13). TbMscL L89 is located at the entrance of the pockets and is structurally aligned
357 to EcMscL M94 and in close proximity to I92, F93, I96 and K97, modifications of which, influence
358 MscL's activation by ultrasound pulses (65), decrease its tension threshold for use in a
359 multicompartmental lipid vesicle framework (66), and modulate its function (12) . Molecules specific
360 to MscL are expected to act through disruption of lipid-protein interactions (26) within these pockets.
361 These did not fully open the channel, but caused a structural rearrangement of TM2's cytoplasmic
362 side accompanied by stretching of the cytoplasmic loop (12, 13). This is in agreement with the
363 structural changes observed by HDX and ESEEM for the modified L89W TbMscL channel (or the
364 structurally equivalent M94 EcMscL) and the tension activated WT channel (Fig 1,3,4,7 and S4).
365 V21 exposure increase in the expanded (by molecular means) MscL state is consistent with a
366 channel pore hydration and opening. N13R1's side chain sits one and two turn(s) of a helix below
367 V17 and V21 on TM1 respectively. N13 is already exposed in the closed state, due to its side chain
368 being solvent accessible (Fig S2 and S3), thus unaffected in the expanded L89W modified state.
369 Transition to a sub-conducting state (L89W in DDM) increased solvent accessibility on the upper
370 TM1 and TM2 and the cytoplasmic loops on top of the helical bundle (Fig 1 and 2). Widening of
371 MscL's cytoplasmic interface causes a stretching of the loops, of which shortening or modification
372 has been shown to influence MscL's gating properties, pore conductance and oligomeric assembly
373 (13, 34, 58, 67, 68).
374 The top of TM1 (residues 36 - 41) partially unfolds within a single subunit of the MscL pentamer,
375 while the remaining four subunits bend without fully converting into a loop. This finding was
376 consistently observed across all three MD simulation repeats following the symmetric application
377 of tension along the membrane xy plane and suggests the presence of a subunit asymmetry during
378 MscL opening (33, 69). In contrast to the WT channel, all five TM1 helices bend without a break in
379 helical symmetry or conversion into a loop in the L89W channel (Fig 4). For the top of TM1 helix to
380 partially unfold, lipids should become loosely associated with the pockets before asymmetric
381 opening could occur and eventually lead to channel opening. A similar activation mechanism has
382 been suggested for the small conductance MS channel MscS where inner-leaflet lipids residing
383 within TM pockets are required to move before outer-leaflet lipids can disengage to allow gating
384 (25). Whether the lipids are sequentially released (or loosen their contact) following single subunit
385 activation remains to be elucidated. Our data are compatible with such an asymmetry in opening
386 and this structural effect may be the consequence of lipids moving out from MscL's five pockets
387 sequentially. Subsequently, following initial expansion and conversion into loops, these loops could
388 then provide membrane handles for MscL in order to transit to its full opening state (Video S1).
389 Despite a significant membrane thinning (~1.2 nm), L89W's pore cannot allow water molecules to
390 flow through (Fig 4). Membrane thickness and hydrophobic mismatch energetically contribute to
391 MscL's gating, but our data suggest they may not be the sole driving force and pocket lipids have
392 to be released first in order to destabilize MscL's closed state. However, we should note that while
393 tension application and channel gating occurs within the 300 ns that our simulations run, this may
394 be faster compared to the timescale of MscL opening transitions.
395 Molecular activation due to binding of molecules acts in domains which are important for lipid-
396 protein interactions and are highly sensitive to membrane tension. Lipids must adopt certain angles
397 in respect to the membrane plane in order to enter (or exit) the pockets and these angles should
398 be consistent with lipids oriented horizontally, contrary to the bulk bilayer lipids. Such lipids have
399 been resolved in multiple x-ray and cryoEM structures of MscS (5, 25), TRAAK (23), TREK-2 (24)
400 and TRPV3 (22) channels. When we calculated the lipid order parameters for our MD simulations,
401 we found that under tension application the lipids adopt a substantially more horizontal orientation
402 (Fig S6). This is consistent with significantly lower pulling forces required to remove single lipids
403 from TbMscL's pockets when they are applied at 45° in respect to the membrane plane (70). Such
404 lipid rearrangement may be part of the closed-closed expansion gating process, since the overall
405 RMSD between the L89W and WT structures following tension application was small, while both
406 differ significant from the closed state (PDB 2OAR) (Fig 7B and S4). These findings are consistent
407 with the pocket lipids acting as negative allosteric modulators . Shifting of the equilibrium occurs in

408 order to destabilize the closed state and initiate symmetric (simultaneous) or asymmetric
409 (sequential) pocket lipid removal from the five MscL subunits (2, 69).
410 Accumulatively, our structural, biophysical and computational data demonstrate that MscL state
411 derived by modification of pressure sensitive TM regions is analogous to the tension activated MscL
412 state (mechanical), summarized in our proposed model (Fig 7C). We generated tension- and
413 modification- activated MscL states and interrogated their pore hydration properties, lipid-protein
414 interactions and monitored their structural dynamics by experimental (HDX-MS and 3pESEEM
415 solvent accessibility measurements) and computational (MD simulations) tools. The structural
416 similarities of these two derived states suggests that molecular triggers could act on specific sites
417 of MscL to mimic naturally occurring tension activation, with implications for the multimodality and
418 ligand activation of MS channels.
419
420 **Materials and Methods**
421
422 For *Materials see* the *SI Appendix*
423
424 Mutagenesis and Protein Expression
425 For detailed protocols *see* the *SI Appendix*
426
427 Protein Purification and Spin Labelling
428 The protocols followed in this study were similar to the ones previously described (2, 15, 54). For
429 details and also HDX-MS sample preparation *see* the *Appendix*.
430
431 3pESEEM spectroscopy
432 X-band three pulse ESEEM measurements were performed on a Bruker ELEXSYS E580
433 spectrometer with a 4 mm dielectric resonator (MD4). Measurements were conducted at 80 K. The
434 3-pulse sequence used for the experiments is $\pi/2$-τ-$\pi/2$-T-$\pi/2$-stimulated echo with a pulse length
435 $t_{\pi/2}$ = 16 ns and inter-pulse delay τ that was adjusted to match either the blind spots of the proton
436 or deuterium. The delay T was incremented from 400ns in 12 ns steps. A four-step phase cycling
437 was used to eliminate the unwanted echoes. All the measurements were performed at the
438 maximum of the filed sweep spectrum of the nitroxide. For solvent accessibility determination, only
439 -3pESEEM data recorded with τ that corresponds to the proton blind spot were used. The obtained
440 time-domain traces were background-corrected, apodized with a hamming window and zero-filled
441 prior to Fourier transformation. The solvent accessibility can be determined either from the
442 modulation depth in time domain or the corresponding amplitude of the deuterium peak in
443 frequency domain. In the present work, the modulation depth for each mutant was determined by
444 fitting the corresponding time-domain trace by a damped harmonic oscillation function and the
445 outcome from the fitting was used to estimate the solvent accessibility (47).
446
447 HDX and LC-MS/MS
448 HDX-MS experiments were carried out using an automated HDX robot (LEAP Technologies, Fort
449 Lauderdale, FL, USA) coupled to an M-Class Acquity LC and HDX manager (Waters Ltd.,
450 Wilmslow, Manchester, UK). All samples were diluted to 16 µM in equilibration buffer (50 mM
451 potassium phosphate, 300 mM NaCl, pH 7.4, 0.05% DDM) prior to analysis. 5 µL sample was
452 added to 95 µl deuterated buffer (50 mM potassium phosphate, 300 mM NaCl pD 7.4, 0.05% DDM)
453 and incubated at 4 °C for 0.5, 1, 2, 10 or 60 min. Following the labelling reaction, samples were
454 quenched by adding 50 µl of the labelled solution to 100 µl quench buffer (50 mM potassium
455 phosphate, 300 mM NaCl, 0.1% DDM pH 2.2) giving a final quench pH ~2.5. 50 µl of quenched
456 sample was injected on to the HDX Manger and passed through immobilized pepsin and
457 aspergillopepsin columns connected in series (AffiPro, Czech Republic) at 115 µl min-1 (20 °C)
458 and loaded on to a VanGuard Pre-column Acquity UPLC BEH C18 (1.7 µm, 2.1 mm X 5 mm,
459 Waters Ltd., Wilmslow, Manchester, UK) for 3 mins in 0.3 % formic acid in water. The resulting
460 peptides were transferred to a C18 column (75 µm X 150 mm, Waters Ltd., Wilmslow, Manchester,

UK) and separated by gradient elution of 0-40 % MeCN (0.1 % v/v formic acid) in H2O (0.3 % v/v formic acid) over 7 mins at 40 µl min-1. Trapping and gradient elution of peptides was performed at 0 oC to reduce back exchange. The HDX system was interfaced to a Synapt G2Si mass spectrometer (Waters Ltd., Wilmslow, Manchester, UK). HDMSE and dynamic range extension modes (Data Independent Analysis (DIA) coupled with IMS separation) were used to separate peptides prior to CID fragmentation in the transfer cell (71). HDX data were analyzed using PLGS (v3.0.2) and DynamX (v3.0.0) software supplied with the mass spectrometer. Restrictions for identified peptides in DynamX were as follows: minimum intensity: 1000, minimum products per MS/MS spectrum: 5, minimum products per amino acid: 0.3, maximum sequence length: 25, maximum ppm error: 5, file threshold: 3/3. Following manual curation of the data, PAVED(72) and Deuteros (52) were used to identify peptides with statistically significant increases/decreases in deuterium uptake (applying 99% or 95% confidence intervals) and to prepare Wood's plots. The raw HDX-MS data, have been deposited to the ProteomeXchange Consortium via the PRIDE partner repository with the dataset identifier PXD021983. A summary of the HDX-MS data, as recommended by reporting guidelines, is shown in Table S1.

Atomistic Molecular Dynamics Simulations

MD simulations under no tension: The set up and parameters of MD simulations without tension were as previously described (2). For more details *see* the *SI Appendix*.

MD simulations under tension: These MD simulations were also set up using CHARMM-GUI (73). The MscL structure (PDB 2OAR) in the wild type and in a mutated form (L89W) was inserted in a symmetric bilayer containing 514 POPC lipids. Systems were neutralized with a 150 mM concentration of NaCl. The obtained system was energy minimised for 5000 steps and subsequently equilibrated in 6 steps following CHARMM-GUIs equilibration. Stretch-induced conformational changes in the MscL model were investigated by unrestrained simulations of 300 ns (3 simulation repeats for each system) were the bilayer plane (xy plane) pressure was changed semiisotropically to -50 bars (which corresponds to a tension of ~67.5 mN/m). The pressure in the bilayer normal (z direction) was kept at +1 bar. All the atomistic systems were simulated using GROMACS 2016 (74) with CHARMM36 force field (75) and a 2 fs time step. The Nose-Hoover thermostat (76) and the Parrinello-Rahman barostat(77) were used for the stretch-induced simulations. All simulations were performed at 310 K. Long-range electrostatics were managed using the particle-mesh Ewald method(78) and the LINCS algorithm was used to constrain bond lengths(79).

Data accessibility

HDX mass spectrometry:

Data are available via ProteomeXchange with identifier PXD021983.

Project Name: Mechanical and molecular activation lead to structurally analogous MscL states

Project accession: PXD021983

Account details: Username: reviewer_pxd021983@ebi.ac.uk, Password: lnAkk2H3

3pESEEM and MD:

Data are available within the following link: http://archive.researchdata.leeds.ac.uk/777/

Acknowledgments

This project was supported by a Biotechnology and Biological Sciences Research Council (BBSRC) grant (BB/S018069/1) to C.P., who also acknowledges support from the Wellcome Trust (WT) (219999/Z/19/Z) and the Chinese Scholarship Council (CSC) in the form of studentships for B.J.L. and B.W. respectively. ANC is a Sir Henry Dale Fellow jointly funded by the WT and the Royal Society (220628/Z/20/Z). Funding from the BBSRC (BB/M012573/1) enabled the purchase of mass spectrometry equipment.

References

1. Laganowsky A, et al. (2014) Membrane proteins bind lipids selectively to modulate their structure and function. Nature 510(7503):172-175.
2. Kapsalis C, et al. (2019) Allosteric activation of an ion channel triggered by modification of mechanosensitive nano-pockets. Nat Commun 10(1):4619.
3. Pliotas C & Naismith JH (2016) Spectator no more, the role of the membrane in regulating ion channel function. Curr Opin Struct Biol 45:59-66.
4. Patrick JW, et al. (2018) Allostery revealed within lipid binding events to membrane proteins. Proc Natl Acad Sci U S A 115(12):2976-2981.
5. Pliotas C, et al. (2015) The role of lipids in mechanosensation. Nat Struct Mol Biol 22(12):991-998.
6. Teng J, Loukin S, Anishkin A, & Kung C (2015) The force-from-lipid (FFL) principle of mechanosensitivity, at large and in elements. Pflugers Arch 467(1):27-37.
7. Malcolm HR, Blount P, & Maurer JA (2015) The mechanosensitive channel of small conductance (MscS) functions as a Jack-in-the box. Biochim Biophys Acta 1848(1 Pt A):159-166.
8. Cox CD, Nakayama Y, Nomura T, & Martinac B (2015) The evolutionary 'tinkering' of MscS-like channels: generation of structural and functional diversity. Pflugers Arch 467(1):3-13.
9. Brohawn SG (2015) How ion channels sense mechanical force: insights from mechanosensitive K2P channels TRAAK, TREK1, and TREK2. Annals of the New York Academy of Sciences 1352:20-32.
10. Naismith JH & Booth IR (2012) Bacterial mechanosensitive channels--MscS: evolution's solution to creating sensitivity in function. Annual review of biophysics 41:157-177.
11. Wray R, Wang J, Iscla I, & Blount P (2020) Novel MscL agonists that allow multiple antibiotics cytoplasmic access activate the channel through a common binding site. PLoS One 15(1):e0228153.
12. Wray R, Iscla I, Kovacs Z, Wang J, & Blount P (2019) Novel compounds that specifically bind and modulate MscL: insights into channel gating mechanisms. FASEB journal : official publication of the Federation of American Societies for Experimental Biology 33(3):3180-3189.
13. Wray R, et al. (2016) Dihydrostreptomycin Directly Binds to, Modulates, and Passes through the MscL Channel Pore. PLoS biology 14(6):e1002473.
14. Rasmussen T, et al. (2019) Interaction of the Mechanosensitive Channel, MscS, with the Membrane Bilayer through Lipid Intercalation into Grooves and Pockets. J Mol Biol 431(17):3339-3352.
15. Kapsalis C, Ma Y, Bode BE, & Pliotas C (2020) In-Lipid Structure of Pressure-Sensitive Domains Hints Mechanosensitive Channel Functional Diversity. Biophys J 119(2):448-459.
16. Syeda R, et al. (2015) Chemical activation of the mechanotransduction channel Piezo1. Elife 4.
17. Botello-Smith WM, et al. (2019) A mechanism for the activation of the mechanosensitive Piezo1 channel by the small molecule Yoda1. Nat Commun 10(1):4503.
18. Bagriantsev SN, Peyronnet R, Clark KA, Honore E, & Minor DL, Jr. (2011) Multiple modalities converge on a common gate to control K2P channel function. EMBO J 30(17):3594-3606.
19. Li B, Rietmeijer RA, & Brohawn SG (2020) Structural basis for pH gating of the two-pore domain K(+) channel TASK2. Nature 586(7829):457-462.
20. Piechotta PL, et al. (2011) The pore structure and gating mechanism of K2P channels. EMBO J 30(17):3607-3619.
21. Feliciangeli S, Chatelain FC, Bichet D, & Lesage F (2015) The family of K2P channels: salient structural and functional properties. J Physiol 593(Pt 12):2587-2603.
22. Deng Z, et al. (2020) Gating of human TRPV3 in a lipid bilayer. Nat Struct Mol Biol.
23. Brohawn SG, Campbell EB, & MacKinnon R (2014) Physical mechanism for gating and mechanosensitivity of the human TRAAK K+ channel. Nature 516(7529):126-130.
24. Dong YY, et al. (2015) K2P channel gating mechanisms revealed by structures of TREK-2 and a complex with Prozac. Science 347(6227):1256-1259.

25.Rasmussen T, Flegler VJ, Rasmussen A, & Bottcher B (2019) Structure of the Mechanosensitive Channel MscS Embedded in the Membrane Bilayer. J Mol Biol.
26.Bavi N, et al. (2016) The role of MscL amphipathic N terminus indicates a blueprint for bilayer-mediated gating of mechanosensitive channels. Nature Communications 7.
27.Erdogmus S, et al. (2019) Helix 8 is the essential structural motif of mechanosensitive GPCRs. Nat Commun 10(1):5784.
28.Debruycker V, et al. (2020) An embedded lipid in the multidrug transporter LmrP suggests a mechanism for polyspecificity. Nat Struct Mol Biol 27(9):829-835.
29.Martinac AD, Bavi N, Bavi O, & Martinac B (2017) Pulling MscL open via N-terminal and TM1 helices: A computational study towards engineering an MscL nanovalve. PLoS One 12(8):e0183822.
30.Gullingsrud J & Schulten K (2003) Gating of MscL studied by steered molecular dynamics. Biophys J 85(4):2087-2099.
31.Bavi N, et al. (2017) Nanomechanical properties of MscL alpha helices: A steered molecular dynamics study. Channels (Austin) 11(3):209-223.
32.Jeon J & Voth GA (2008) Gating of the mechanosensitive channel protein MscL: the interplay of membrane and protein. Biophys J 94(9):3497-3511.
33.Konijnenberg A, et al. (2014) Global structural changes of an ion channel during its gating are followed by ion mobility mass spectrometry. Proc Natl Acad Sci U S A 111(48):17170-17175.
34.Herrera N, Maksaev G, Haswell ES, & Rees DC (2018) Elucidating a role for the cytoplasmic domain in the Mycobacterium tuberculosis mechanosensitive channel of large conductance. Scientific reports 8(1):14566.
35.Mukherjee N, et al. (2014) The activation mode of the mechanosensitive ion channel, MscL, by lysophosphatidylcholine differs from tension-induced gating. FASEB journal : official publication of the Federation of American Societies for Experimental Biology 28(10):4292-4302.
36.Katsuta H, Sawada Y, & Sokabe M (2019) Biophysical Mechanisms of Membrane-Thickness-Dependent MscL Gating: An All-Atom Molecular Dynamics Study. Langmuir 35(23):7432-7442.
37.Sawada Y & Sokabe M (2015) Molecular dynamics study on protein-water interplay in the mechanogating of the bacterial mechanosensitive channel MscL. Eur Biophys J 44(7):531-543.
38.Sawada Y, Murase M, & Sokabe M (2012) The gating mechanism of the bacterial mechanosensitive channel MscL revealed by molecular dynamics simulations: from tension sensing to channel opening. Channels (Austin) 6(4):317-331.
39.Aryal P, et al. (2017) Bilayer-Mediated Structural Transitions Control Mechanosensitivity of the TREK-2 K2P Channel. Structure 25(5):708-718.e702.
40.Martens C, Shekhar M, Lau AM, Tajkhorshid E, & Politis A (2019) Integrating hydrogen-deuterium exchange mass spectrometry with molecular dynamics simulations to probe lipid-modulated conformational changes in membrane proteins. Nat Protoc 14(11):3183-3204.
41.Ahdash Z, et al. (2019) HDX-MS reveals nucleotide-dependent, anti-correlated opening and closure of SecA and SecY channels of the bacterial translocon. Elife 8.
42.Konermann L, Pan J, & Liu YH (2011) Hydrogen exchange mass spectrometry for studying protein structure and dynamics. Chem Soc Rev 40(3):1224-1234.
43.Moller IR, et al. (2019) Conformational dynamics of the human serotonin transporter during substrate and drug binding. Nat Commun 10(1):1687.
44.Martens C, et al. (2018) Direct protein-lipid interactions shape the conformational landscape of secondary transporters. Nat Commun 9(1):4151.
45.Cieslak JA, Focia PJ, & Gross A (2010) Electron spin-echo envelope modulation (ESEEM) reveals water and phosphate interactions with the KcsA potassium channel. Biochemistry 49(7):1486-1494.
46.Pliotas C (2017) Ion Channel Conformation and Oligomerization Assessment by Site-Directed Spin Labeling and Pulsed-EPR. Methods in enzymology 594:203-242.
47.Volkov A, Dockter C, Bund T, Paulsen H, & Jeschke G (2009) Pulsed EPR determination of water accessibility to spin-labeled amino acid residues in LHCIIb. Biophys J 96(3):1124-1141.
48.Liu L, et al. (2016) Probing the Local Secondary Structure of Human Vimentin with Electron Spin Echo Envelope Modulation (ESEEM) Spectroscopy. J Phys Chem B 120(48):12321-12326.

622 49.Zhang R, et al. (2015) Development of electron spin echo envelope modulation spectroscopy
623 to probe the secondary structure of recombinant membrane proteins in a lipid bilayer. Protein Sci
624 24(11):1707-1713.
625 50.Matalon E, et al. (2013) Topology of the trans-membrane peptide WALP23 in model membranes
626 under negative mismatch conditions. J Phys Chem B 117(8):2280-2293.
627 51.Hartley AM, Ma Y, Lane BJ, Wang B, & Pliotas C (2021) Using pulsed EPR in the structural
628 analysis of integral membrane proteins. Electron Paramag Reson 27:74 -108.
629 52.Lau AMC, Ahdash Z, Martens C, & Politis A (2019) Deuteros: software for rapid analysis and
630 visualization of data from differential hydrogen deuterium exchange-mass spectrometry.
631 Bioinformatics 35(17):3171-3173.
632 53.Bavi N, et al. (2016) The role of MscL amphipathic N terminus indicates a blueprint for bilayer-
633 mediated gating of mechanosensitive channels. Nat Commun 7:11984.
634 54.Michou M, Kapsalis C, Pliotas C, & Skretas G (2019) Optimization of Recombinant Membrane
635 Protein Production in the Engineered Escherichia coli Strains SuptoxD and SuptoxR. ACS Synth
636 Biol 8(7):1631-1641.
637 55.Chang G, Spencer RH, Lee AT, Barclay MT, & Rees DC (1998) Structure of the MscL homolog
638 from Mycobacterium tuberculosis: a gated mechanosensitive ion channel. Science
639 282(5397):2220-2226.
640 56.Li J, et al. (2015) Mechanical coupling of the multiple structural elements of the large-
641 conductance mechanosensitive channel during expansion. Proc Natl Acad Sci U S A
642 112(34):10726-10731.
643 57.Powl AM, East JM, & Lee AG (2005) Heterogeneity in the binding of lipid molecules to the
644 surface of a membrane protein: Hot spots for anionic lipids on the mechanosensitive channel of
645 large conductance MscL and effects on conformation. Biochemistry 44(15):5873-5883.
646 58.Yang LM, et al. (2012) Three routes to modulate the pore size of the MscL channel/nanovalve.
647 ACS Nano 6(2):1134-1141.
648 59.Klesse G, Rao S, Sansom MSP, & Tucker SJ (2019) CHAP: A Versatile Tool for the Structural
649 and Functional Annotation of Ion Channel Pores. J Mol Biol 431(17):3353-3365.
650 60.Smart OS, Goodfellow JM, & Wallace BA (1993) The pore dimensions of gramicidin A. Biophys
651 J 65(6):2455-2460.
652 61.Clausen MV, Jarerattanachat V, Carpenter EP, Sansom MSP, & Tucker SJ (2017) Asymmetric
653 mechanosensitivity in a eukaryotic ion channel. Proc Natl Acad Sci U S A.
654 62.Betanzos M, Chiang CS, Guy HR, & Sukharev S (2002) A large iris-like expansion of a
655 mechanosensitive channel protein induced by membrane tension. Nature structural biology
656 9(9):704-710.
657 63.Boucher PA, Morris CE, & Joos B (2009) Mechanosensitive closed-closed transitions in large
658 membrane proteins: osmoprotection and tension damping. Biophys J 97(10):2761-2770.
659 64.Iscla I, Wray R, Wei S, Posner B, & Blount P (2014) Streptomycin potency is dependent on
660 MscL channel expression. Nat Commun 5:4891.
661 65.Ye J, et al. (2018) Ultrasonic Control of Neural Activity through Activation of the
662 Mechanosensitive Channel MscL. Nano Lett 18(7):4148-4155.
663 66.Hindley JW, et al. (2019) Building a synthetic mechanosensitive signaling pathway in
664 compartmentalized artificial cells. Proc Natl Acad Sci U S A 116(34):16711-16716.
665 67.Reading E, et al. (2015) The Effect of Detergent, Temperature, and Lipid on the Oligomeric
666 State of MscL Constructs: Insights from Mass Spectrometry. Chem Biol 22(5):593-603.
667 68.Liu Z, Gandhi CS, & Rees DC (2009) Structure of a tetrameric MscL in an expanded
668 intermediate state. Nature 461(7260):120-124.
669 69.Birkner JP, Poolman B, & Kocer A (2012) Hydrophobic gating of mechanosensitive channel of
670 large conductance evidenced by single-subunit resolution. Proc Natl Acad Sci U S A
671 109(32):12944-12949.
672 70.Vanegas JM & Arroyo M (2014) Force transduction and lipid binding in MscL: a continuum-
673 molecular approach. PLoS One 9(12):e113947.

71. Cryar A, Groves K, & Quaglia M (2017) Online Hydrogen-Deuterium Exchange Traveling Wave Ion Mobility Mass Spectrometry (HDX-IM-MS): a Systematic Evaluation. J Am Soc Mass Spectrom 28(6):1192-1202.
72. Cornwell O, Radford SE, Ashcroft AE, & Ault JR (2018) Comparing Hydrogen Deuterium Exchange and Fast Photochemical Oxidation of Proteins: a Structural Characterisation of Wild-Type and DeltaN6 beta2-Microglobulin. J Am Soc Mass Spectrom 29(12):2413-2426.
73. Jo S, Kim T, Iyer VG, & Im W (2008) CHARMM-GUI: a web-based graphical user interface for CHARMM. Journal of computational chemistry 29(11):1859-1865.
74. Abraham MJ, T. Murtola, R. Schulz, S. Páll, J.C. Smith, B. Hess, E. Lindah, and E. Lindahl (2015) GROMACS: High performance molecular simulations through multi-level parallelism from laptops to supercomputers. SoftwareX 1-2:19-25.
75. Lee S, et al. (2014) CHARMM36 united atom chain model for lipids and surfactants. J Phys Chem B 118(2):547-556.
76. Evans DJ, Holian B.L. (1985) The Nose-Hoover thermostat. J. Chem. Phys. 83:4069–4074.
77. Parrinello M, Rahman A. (1981) Polymorphic transitions in single crystals: A new molecular dynamics method. J. Appl. Phys. 52:7182–7190.
78. Darden T, York, D., Pedersen L. (1993) Particle mesh Ewald: An N·log(N) method for Ewald sums in large systems. J. Chem. Phys. 98:10089–10092.
79. Hess B, H. Bekker, H.J.C. Berendsen, J.G.E.M. Fraaije (1997) INCS: A linear constraint solver for molecular simulations. J. Comput. Chem. 18:1463–1472.

696
697 **Figures and Tables**

698

A

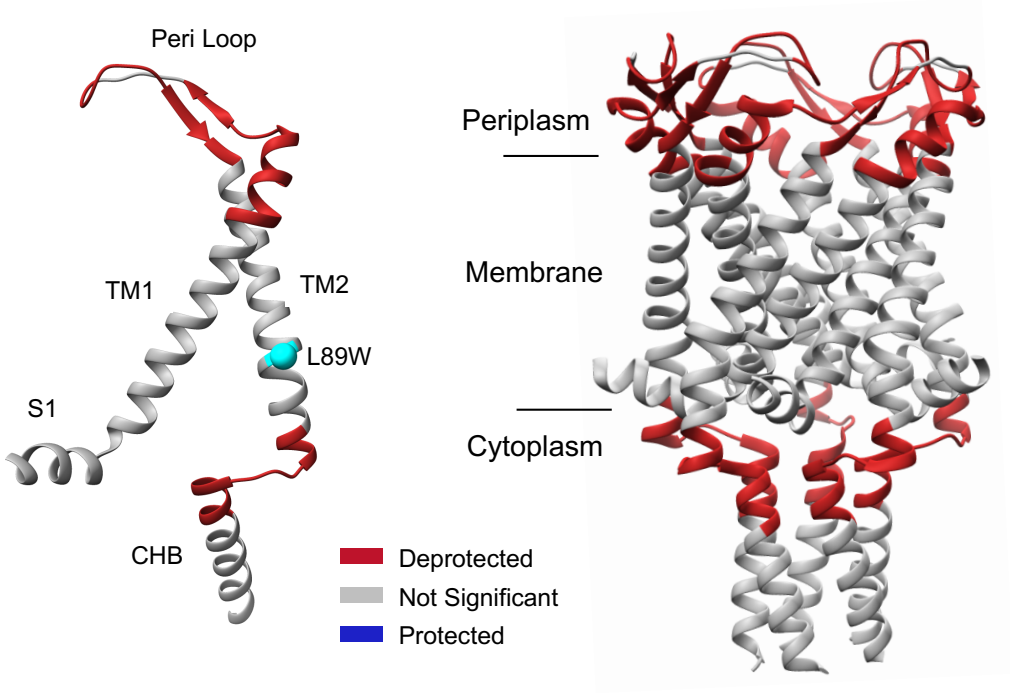

B

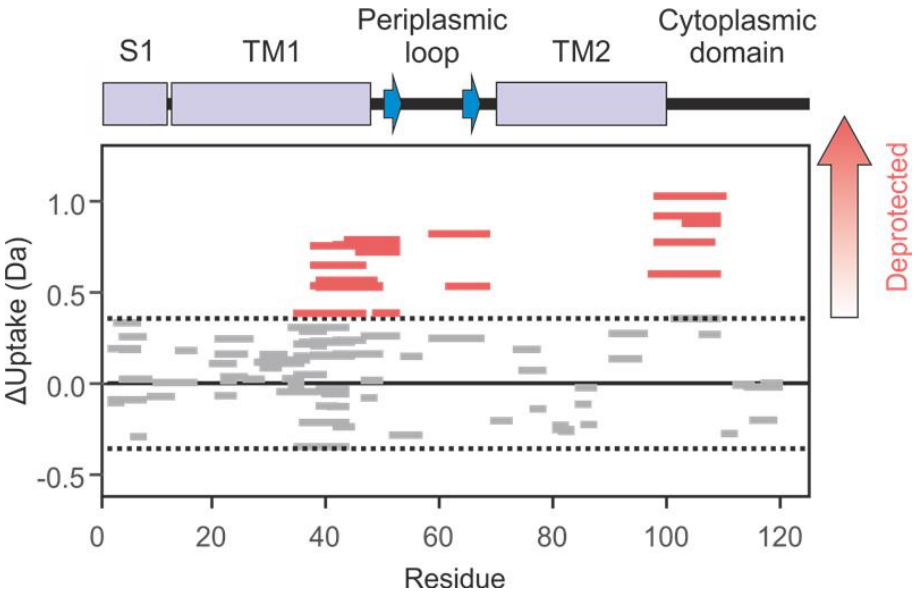

699
700
701
702
703
704
705

706
707
708
709 **Figure 1.** Observed changes in solvent accessibility and secondary structure by HDX-MS following
710 L89W pocket-entrance modification. A. Differences in the deuterium uptake of regions of TbMscL
711 (PDB 2OAR) when comparing the WT and the L89W modified protein. Regions highlighted in red
712 are deprotected following the L89W modification. Regions of the protein in grey show no significant
713 difference between the two conditions. L89W modification site is depicted as a cyan sphere. B.
714 Wood's plots showing the summed differences in deuterium uptake in MscL over all five HDX
715 timepoints, comparing WT with L89W MscL (Wood's plots were generated using Deuteros(52).
716 Peptides coloured in red, are deprotected from exchange in L89W MscL. No peptides were
717 significantly protected from exchange in L89W MscL compared with wild type MscL. Peptides with
718 no significant difference between conditions, determined using a 99% confidence interval (dotted
719 line), are shown in grey. Example deuterium uptake curves are shown in Fig S1.
720

721

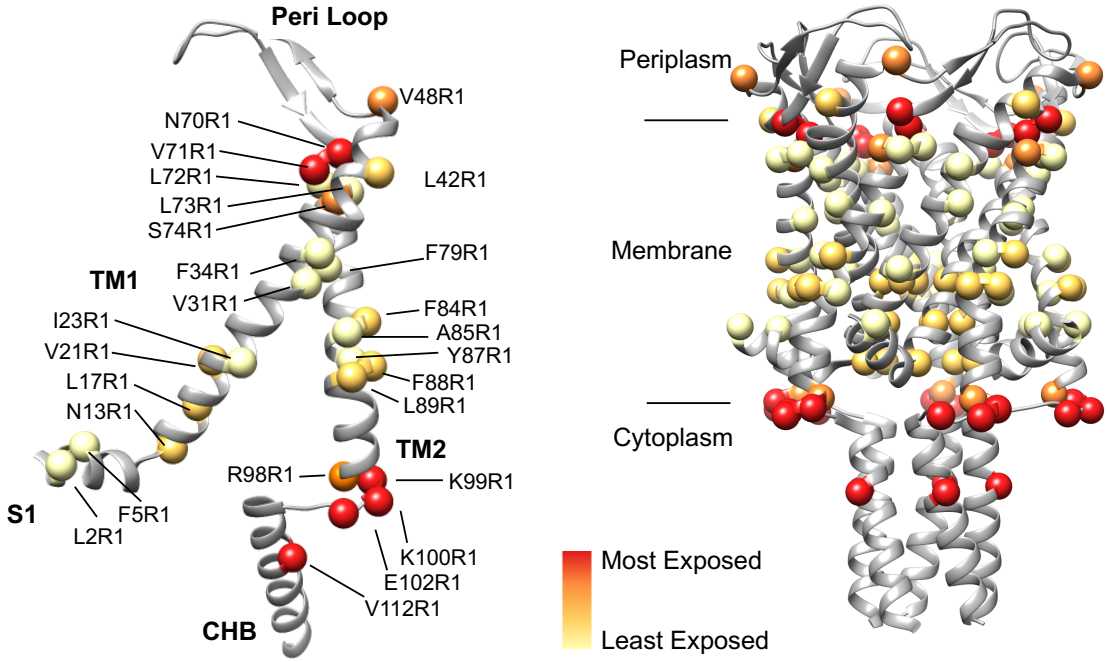

Figure 2. Single residue solvent accessibility mapping of MscL by 3pESEEM. Spin-labelled residues are shown as red and pale yellow spheres for the most and the least solvent accessible residues respectively. Spin-labelled residues are coloured based on the quartile of their relative accessibility which has been normalised on scale of 0% and 100%, where the residues with the highest accessibility corresponds to 100%.

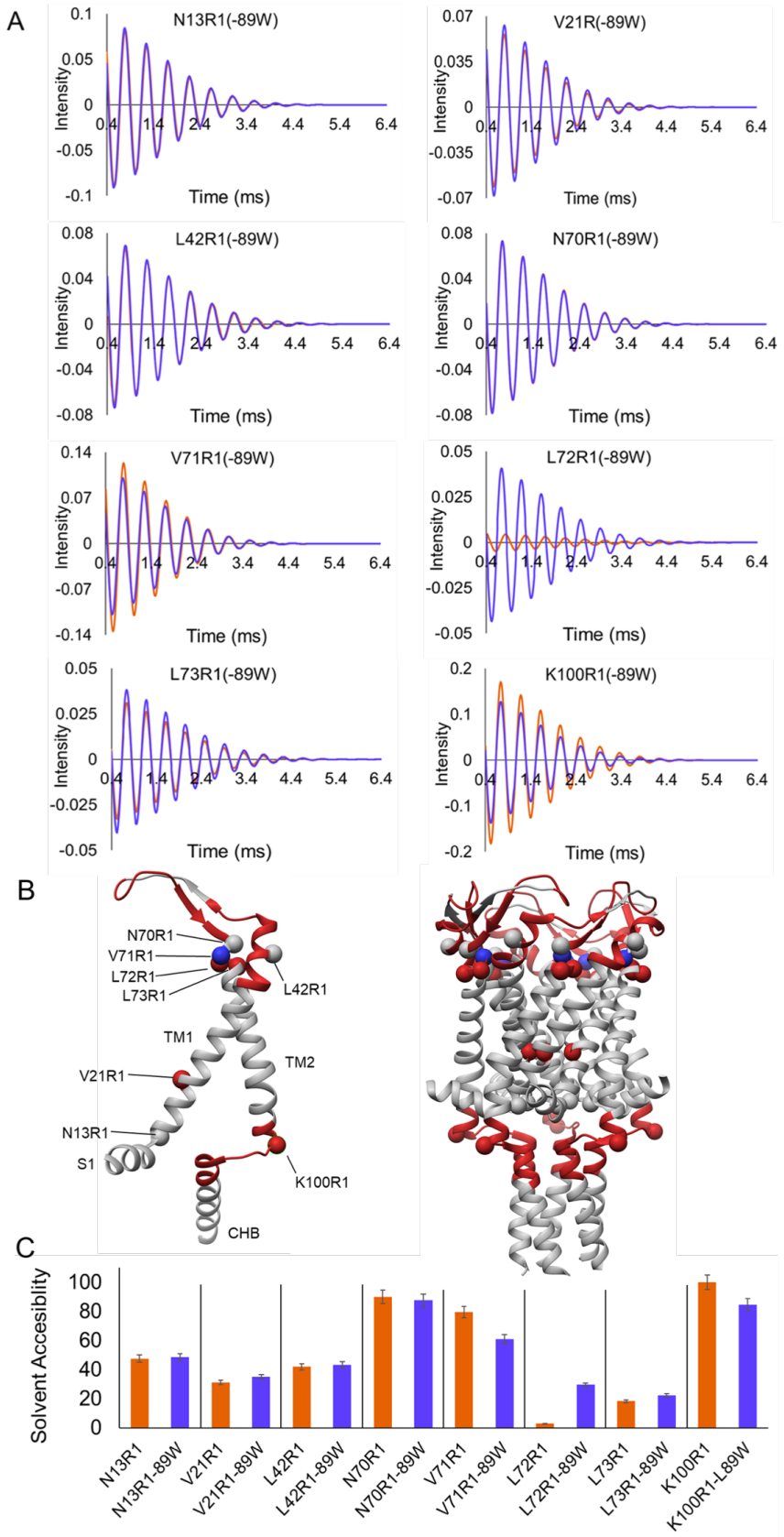
A
N13R1(-89W)
V21R(-89W)
L42R1(-89W)
N70R1(-89W)
V71R1(-89W)
L72R1(-89W)
L73R1(-89W)
K100R1(-89W)
Intensity
Time (ms)
B
N70R1
V71R1
L72R1
L73R1
L42R1
TM1
TM2
V21R1
N13R1
S1
K100R1
CHB
C
Solvent Accesiblity
N13R1
N13R1-89W
V21R1
V21R1-89W
L42R1
L42R1-89W
N70R1
N70R1-89W
V71R1
V71R1-89W
L72R1
L72R1-89W
L73R1
L73R1-89W
K100R1
K100R1-L89W

733

734 **Figure 3**. Molecular activation of MscL investigated by integrated 3pESEEM and HDX-MS solvent
735 accessibility measurements. A Time-domain 3pESEEM fitted experimental spectra (orange) of the
736 single mutants N13R1, V21R1, L42R1, N70R1, L72R1, L73R1, and K100R1 in DDM overlaid with
737 the L89W double mutant fitted spectra (purple) (for fitting see Methods). B Differences in solvent
738 accessibility for TbMscL (PDB 2OAR) following L89W modification. Spin labelled mutation sites
739 used for 3pESEEM accessibility measurements are represented by spheres, and peptides that
740 demonstrate a change in accessibility in HDX-MS following the L89W modification are represented
741 as highlighted helices. Red regions or spheres highlight areas that are deprotected, while blue
742 spheres and regions show areas that are protected following the L89W modification C Column bar
743 charts represent the 2H accessibility derived from the fitting of 3pESEEM time-domain traces.
744 Errors are calculated conservatively at 5% to compensate for the fitting error and differences in
745 relaxation times of different spin labelled residues. There was no significant difference in solvent
746 accessibility of N13R1, L42R1, and N70R1 compared to their 89W double mutant counterpart.
747 Solvent accessibility increased for V21R1, L72R1, and decreased for L71R1 and K100R1 following
748 the L89W modification.
749
750

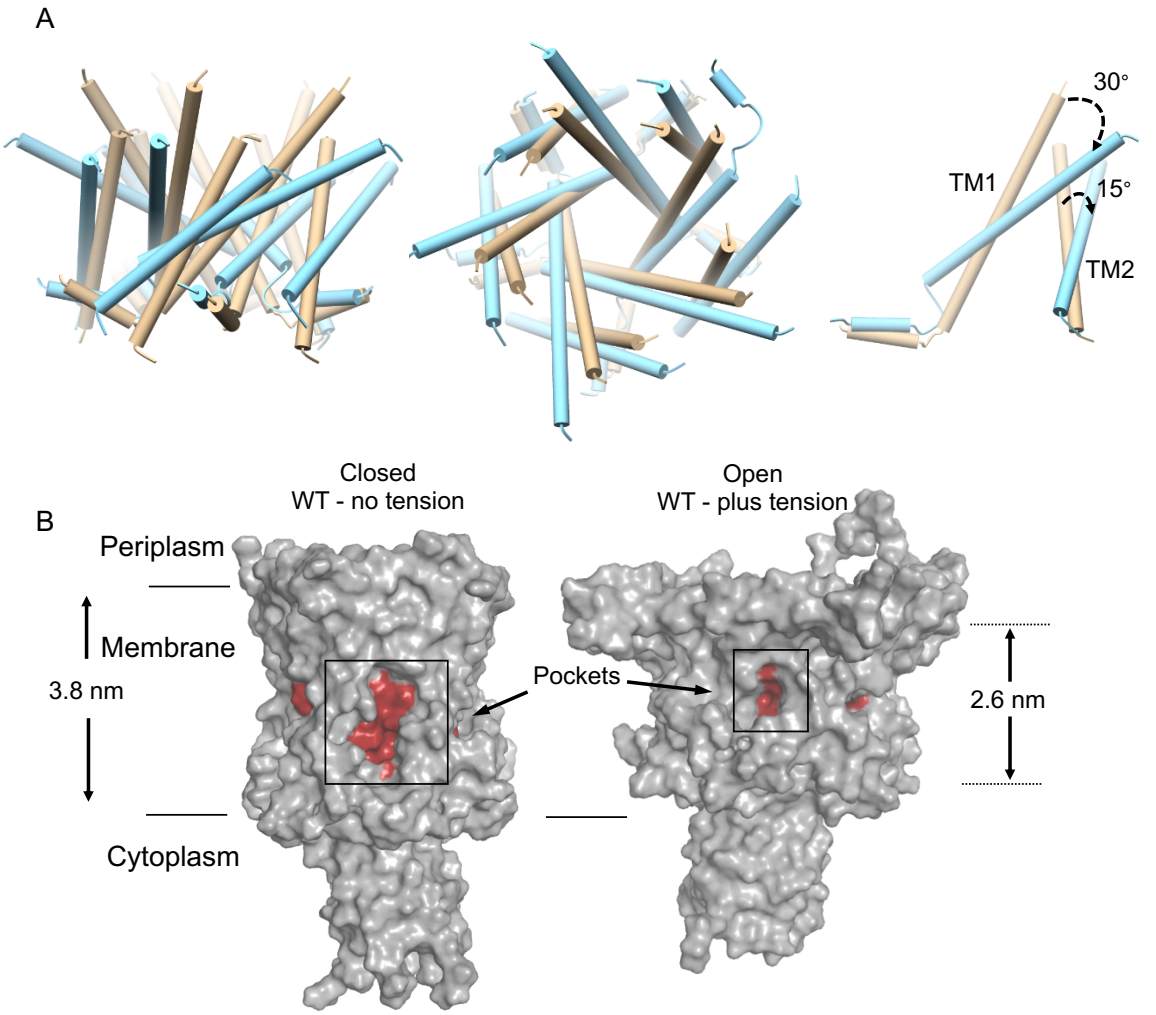

Figure 4. Expanded MscL state under bilayer tension. A. TM comparison between closed TbMscL (tan, PDB 2OAR) and the open state WT MscL generated by MD simulations (cyan, under tension), side, top and single subunit views. The latter shows a substantial tilting of TM1 and TM2 towards the membrane plane. These conformational changes occurring under tension are more evident in Video S1 B The pockets surface dramatically decreases upon tension application, limiting lipid access. Uniform membrane thinning of 1.2 nm (3.8 to 2.6 nm) also occurs during channel expansion, due to tension application.

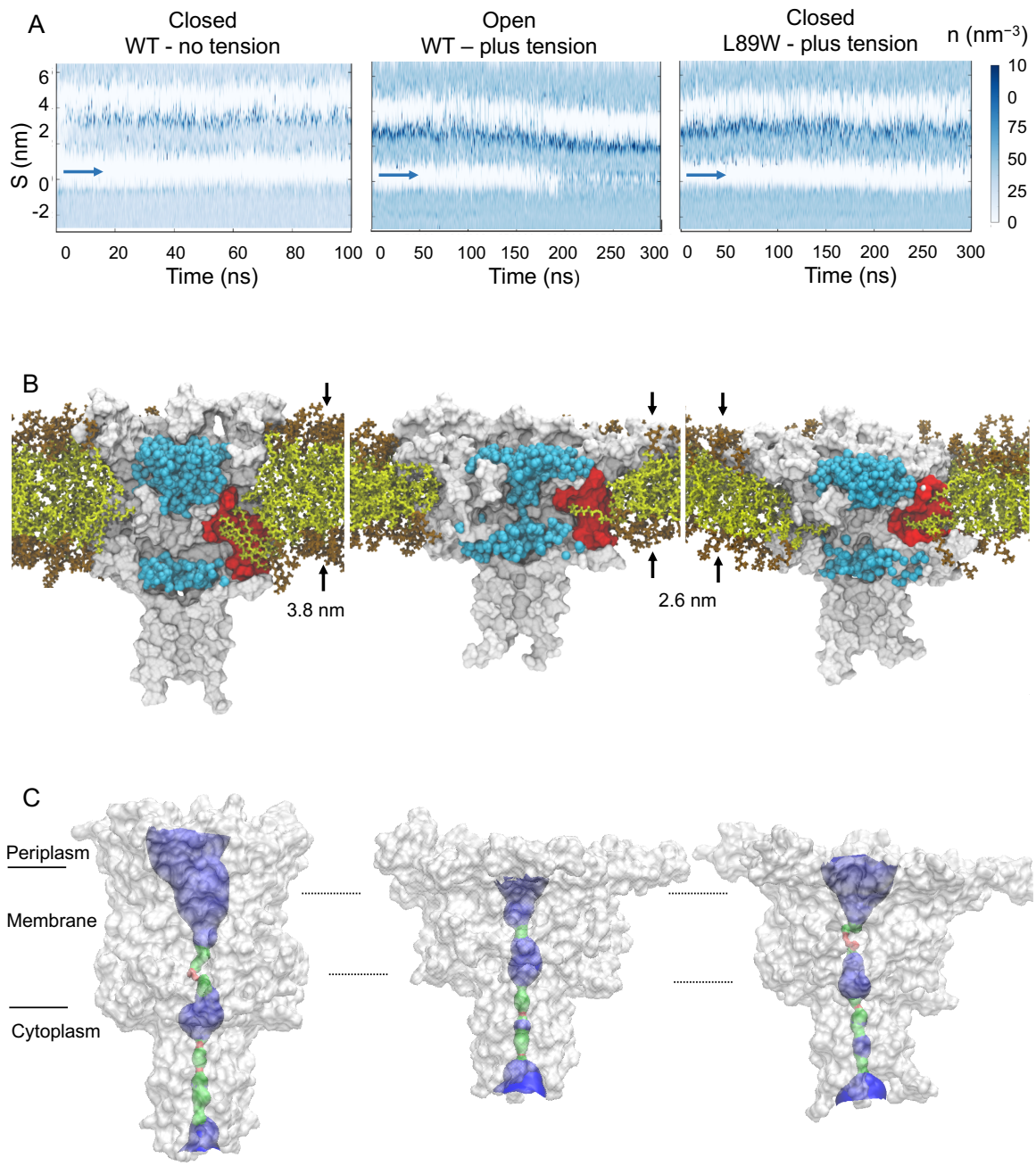
A
Closed
WT - no tension
Open
WT – plus tension
Closed
L89W - plus tension
n (nm^{-3})
S (nm)
Time (ns)
B
3.8 nm
2.6 nm
C
Periplasm
Membrane
Cytoplasm

774
775 **Figure 5**. Pore hydration under applied bilayer tension. WT under no tension (left column), WT
776 under bilayer tension (right column), L89W under bilayer tension (right column). A. Solvent density
777 profile of the MD simulations using the CHAP(59) software with the vapour-lock position of MscL
778 marked with blue arrows. B. Membrane becomes thinner when tension is applied but only the WT
779 TbMscL pore is hydrated (blue spheres) in contrast to L89W channel. Lipid (olive sticks) availability
780 is larger in the closed state, and lipids have easier access within the pockets to provide force on
781 the back of the vapour lock, keeping the MscL pore closed. This is in contrast to WT MscL under
782 tension (middle column) where the pockets become smaller, while lipid availability decreases and
783 the pore becomes hydrated. However, when lipids are trapped in the pockets of the L89W modified
784 channel, the pore does not become hydrated despite structural rearrangements occurring (right
785 column). C. Surface visualization of the pore pathway using the program HOLE(60). Red colour
786 indicates a pore radius smaller than 1.15 Å (water molecules cannot go through such an opening),
787 blue represents a radius larger than 2.3 Å and green between 1.15 to 2.3 Å.
788
789

790
791
792
793
794

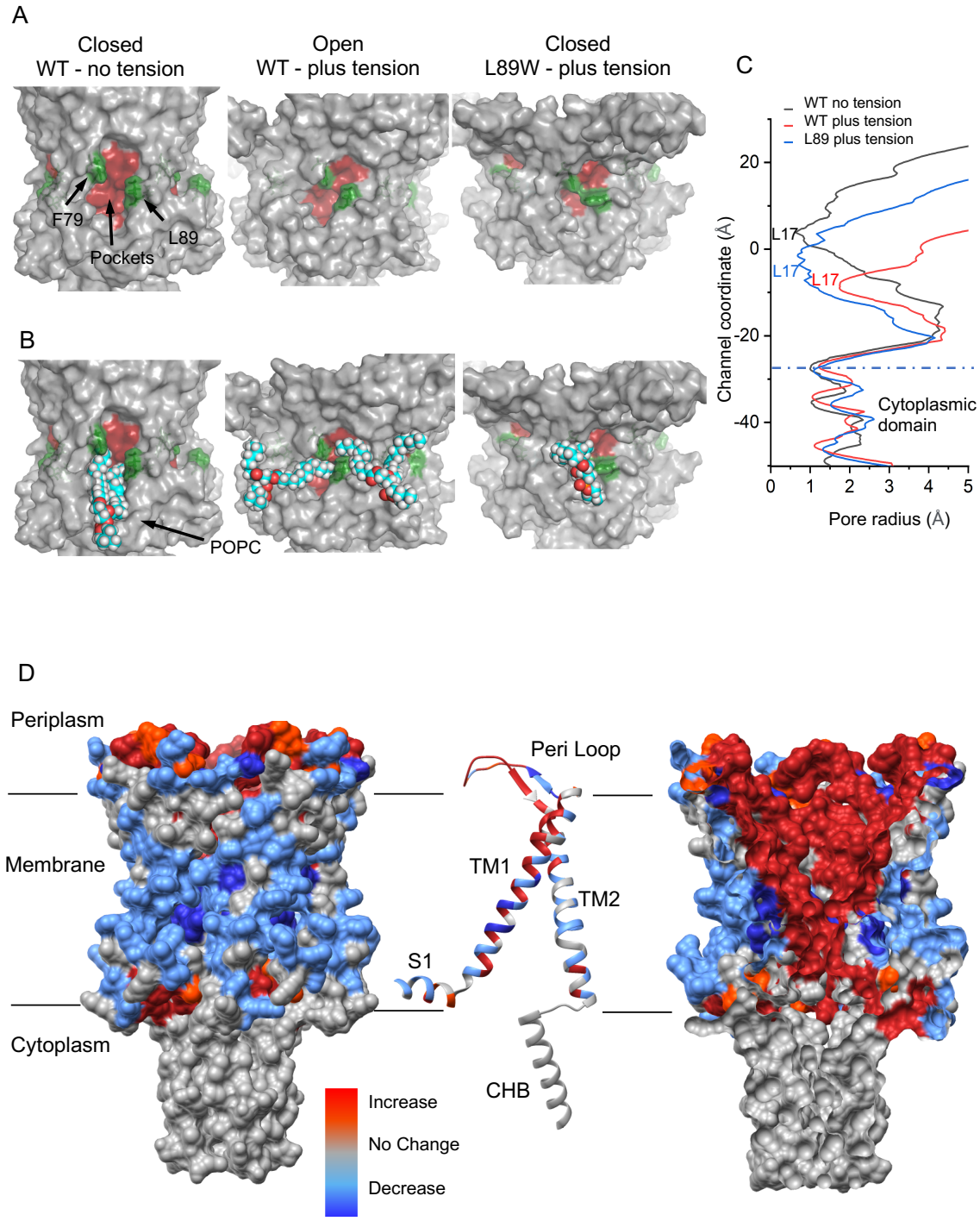

795
796

Figure 6. The effect of membrane tension to MscL lipid contact interactions. (A) and (B). F79 and L89W form a “molecular bridge” in the L89W under tension state and consequently trap the lipids within the pockets (right column). F79 and L89 come into greater proximity under bilayer tension in the WT channel (expanded MscL, middle column) compared to the closed state. However, they do not prevent the lipids from exchanging with the bulk bilayer during tension application. The L89W mutation locks lipids in the pockets, preventing the channel from transiting to a hydrated state. C. MscL pore radius profiles analysis and comparisons using HOLE(60). Although L89W MscL undergoes similar major rearrangements to WT MscL under tension its pore remains significantly smaller and almost identical to WT closed MscL under no tension. D. Relative changes in the number of lipid contacts following stimulated tension in the membrane during MD simulations. The blue regions show decrease in lipid contacts, while the red regions show an increase in lipid contacts. From left to right: Surface view, single subunit cartoon representation and internal MscL surface view. Internal channel regions become more exposed to lipids, while initially membrane exposed regions (closed state) become less exposed to lipids, suggesting a MscL TM helical rotation upon tension application and channel expansion/opening.

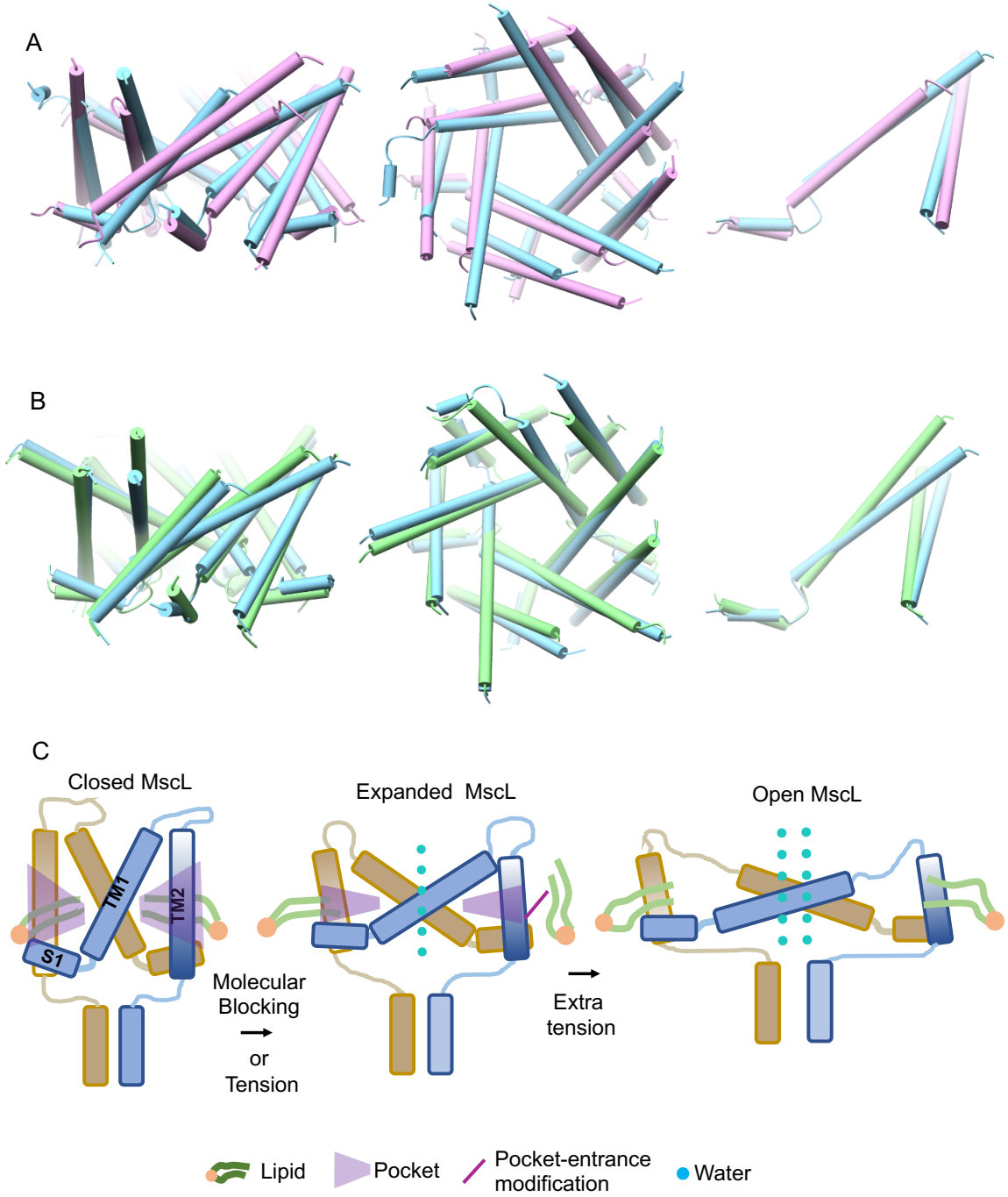

818
819
820
821
822
823
824
825

826 **Figure 7.** Structural comparison between tension and molecular MscL activation and proposed
827 model. TM1 and TM2 tilt and rotate to initiate MscL opening. Comparison between expanded
828 MaMscL (orchid, PDB ID: 4Y7J) and the open state WT TbMscL generated by MD (cyan, under
829 tension) (A) and the open WT TbMscL state generated by MD (cyan, under tesion) and L89W
830 TbMscL (green, under tension) (B). C. Proposed gating model for molecular and tension activated
831 modes. Closed (vertical TM helices, large pockets, tightly associated annular lipids and non-
832 hydrated pore), Expanded (tilted TM helices, smaller pockets, loosely associated annular lipids and
833 hydrated pore). Extra membrane tension is required to fully open MscL.
834
835

836
837
838
839 **Table 1.** Pairwise force energy calculations between TbMscL 89 (L or W) and lipids in the WT (L)
840 and pocket-entrance modified (W) channels and under tension
841
842
843
844
845
846
847
848
849

89 - POPC	Coulomb (KJ/mol)	SD - Coulomb (KJ/mol)	Lennard Jones (KJ/mol)	SD - Lennard Jones (KJ/mol)	Total Energy (KJ/mol)	SD – Total Energy (KJ/mol)
WT	-14.50	1.76	-101.39	27.43	-115.89	29.19
L89W	-14.77	3.90	-192.48	3.39	-207.25	7.29